Transverse Electrokinetic Effect: Experiments and Theory

Chandramouli Subramaniam,[†] T. Pradeep,*[,†] and J. Chakrabarti*[,‡]

DST Unit on Nanoscience (DSTUNS), Department of Chemistry and Sophisticated Analytical Instrument Facility, Indian Institute of Technology Madras, Chennai 600036, India, and S. N. Bose National Centre for Basic Sciences, Block-JD, Sector-III, Salt Lake, Kolkata 700091, India

We observe the transverse electrokinetic effect (TEK), namely, the generation of a transverse potential difference due to the flow of liquids over a surface on which self-assembled arrays of metallic nanoparticles are immobilized. This paper covers the recent experimental findings and improvements to the theoretical model described in ref 1 [Subramaniam, C.; Pradeep, T.; Chakrabarti, J. *Phys. Rev. Lett.* **2005**, *95*, 0164501], leading to a better understanding of the phenomenon. Issues critical for the comprehension and applicability of this effect as a potential flow sensor such as the need for a critical dipole moment, optimum surface coverage, nature of the flow rate dependence, and generalization of the phenomenon for several metallic nanostructures have been addressed in detail from both experimental and theoretical perspectives. This complete work stresses the uniqueness of this new phenomenon which could find applications in emerging areas of science, like microfluidics.

I. Introduction

One of the most widely researched areas of nanomaterials is their ability to act as sensors of a wide range of chemical,[2] biological,[3] and therapeutic agents.[4] Various properties of nanomaterials such as the surface plasmon resonance, photoluminescence, surface enhanced Raman scattering,[5] and electrical properties[6] are vital in their applicability as sensors. These properties can be traced back to the high surface-to-volume ratio of nanomaterials apart from specific aspects of their electronic structure. Translating the detection capabilities of nanoparticles in the solution phase into devices in the solid state has been a challenge. Uniformity of the nanoparticle coverage, stability of the nanoparticles in the solid-state, reproducibility of the response derived, and cross-sensitivity are key issues to be considered while designing a solid-state sensor device. Drop-casting of solutions,[7] chemical vapor deposition,[8,9] template-based patterning,[10] and lithography have been promising techniques toward the development of solid-state devices and sensors. While the first technique suffers from nonuniformity, batch production and cost-effectiveness are important issues in other techniques. Relying on the capabilities of covalent bonds to fabricate stable arrays and surface functionalization to maneuver the surface density of nanoparticles, the vital properties of nanoparticles responsible for the sensor action can be preserved yielding greater reproducibility of the results while providing ease of fabrication. With the assembly formation driven mainly by thermodynamics, defects are lowered.[11] Self-assembled mono- and multilayers of nanoparticles on glass substrates have been used as sensors.[12−14] Substrates like conducting glass, gold film, etc. allow one to monitor the electrical characteristics which are heavily dependent on chemical environment of such an assembly. The functionality of such substrates has been immensely highlighted by reports, concerned with photovoltaic applications. Besides providing electrical conductivity, these substrates are optically transparent and thereby allow one to monitor reaction pathways through spectroscopic techniques.

In the recent past, efforts have been made to develop systems for studying flow through channels. This has been fuelled by the requirements to miniaturize existing devices, leading to the development of a new branch of science known as microfluidics. Indeed, microfluidics and nanotechnology have been complementing each other, with advances in one field leading to newer techniques in the other. Therefore, the demand for development and commercialization of systems to study and control flow is ever-expanding. A review by Nguyen summarizes some of the commercially available flow sensors and their working principles.[15] Besides the technological importance, flow sensing can also be beneficial for studying intrinsic properties of liquid dispersions, like zeta potential, as has been recently demonstrated.[16] Yang et al.[17] show that pressure driven flow of a liquid through narrow pores leads to streaming of electrical double layer, manifested as streaming current.[17] Such a current is found to increase with the increase in ionic concentration, contrary to observations in this report. This was followed by a recent study estimating the efficiency of such a device to function as a battery.[18] Simultaneously, Ghosh et al. reported that flowing fluids through carbon nanotubes resulted in the generation of a potential difference in the direction parallel to the flow.[19,20] Inspired by the theoretical work of Kral et al.,[21] they attributed this effect to the asymmetric ratchet of phonons produced by the flowing liquid as it traverses through the carbon nanotubes.

Earlier work from our group has pointed out the phenomenon of TEK[1] arising from metal nanoparticle assemblies when subjected to liquid flows. The potential difference, generated in the transverse direction to the flow, was dependent on the nature of the flowing liquid and the flow rate. This was in stark contrast to the earlier reports where the potential was developed in a direction parallel to the flow. Therefore, the inherent mechanism responsible for the generation of this potential difference is different from the existing ones. We ascribed this

* To whom correspondence should be addressed. E-mail: pradeep@iitm.ac.in (T.P.); jaydeb@bose.res.in (J.C.).

[†] Indian Institute of Technology Madras.

[‡] S. N. Bose National Centre for Basic Sciences.

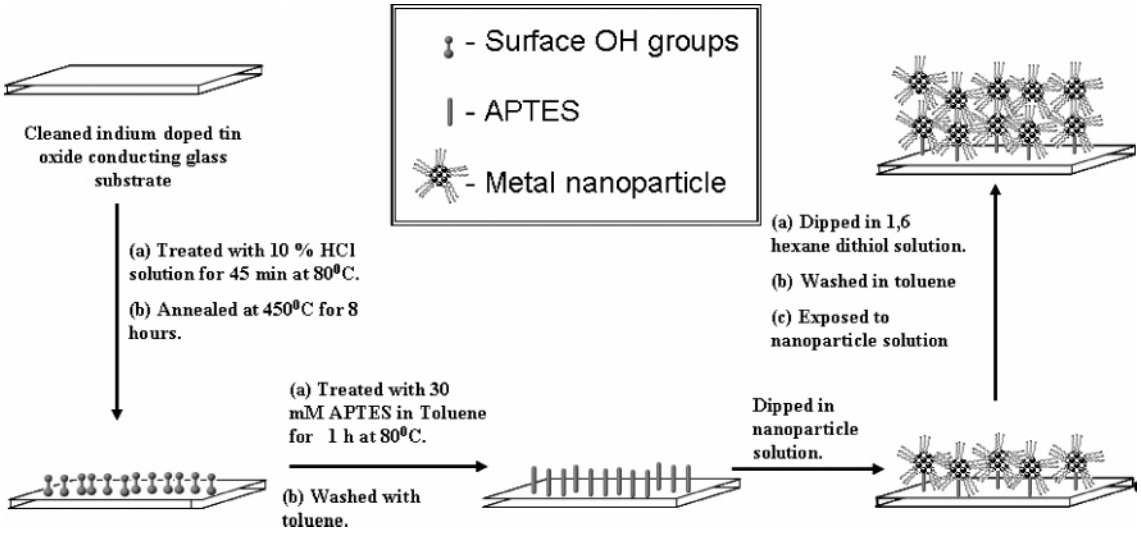

Figure 1. Schematic representation of the multilayer fabrication. The steps of dipping in the nanoparticle dispersion and HDT solution were repeated to obtain the desired surface coverage.

effect as being due to the Coulomb interaction of the dipoles present in the flowing liquid, with the charges present on the surface of metallic nanoparticles. In brief, the Coulomb collisions lead to ejection of the surface charges, leaving the nanoparticles charged. The ejected charges undergo motion due to the coupled effects of the streaming fluid and the electrostatic interaction due to the charged nanoparticles. The generation of the TEK depends crucially on these two competing factors. Fluidic field effect transistors involving the application of a transverse bias to manipulate the flow through microchannels have been envisaged.[22] Such maneuverability and flexibility are deemed to be critical in a microfluidic environment for the control of the flow of the analytes and their subsequent reactions. The TEK may have far-reaching consequences in the development and commercialization of such devices where the microfluidic flow generated the required transverse bias.

In the present work, we have done more elaborate measurements on a variety of nanoparticle systems such as gold nanoparticles (AuNPs), gold nanorods (AuNRs), and silver nanoparticles (AgNPs). The dependence of TEK on various parameters of the analyte liquid has been studied in great detail. These experiments have established certain important aspects of this phenomenon like its sensitivity to the dipole moment of the analyte and surface coverage of nanoparticles. Further, the necessity of a critical dipole moment in order to observe the effect and the nonlinear dependence of the potential difference on the flow rate are conclusions that are of paramount importance to the fundamental understanding of the phenomenon and its practical applicability. TEK was not observed for gas flow, due to the low number density of dipoles which interact effectively with the surface charge. This is an important observation, which proves the uniqueness of this effect when compared to similar reports.[17,19,20] We have presented an improved model with calculations involving the direct flux estimation on the substrate to account for the potential difference observed. A direct comparison between the experimental observations and theoretical predictions could be elucidated through such calculations. These newer aspects of the theoretical model along with their experimental support are discussed in this paper.

The plan of the paper is as follows. In section II, we describe the experimental methods including the sample preparation. The experimental results are detailed in section III. Section IV describes the theoretical model and the results to understand the key features of the experimental observations. We conclude the paper in section V.

II. Experimental Methods

The experimental methods have been broadly categorized in three parts: (1) preparation of nanoparticle coated substrates, (2) characterization of samples, and (3) electrical measurements.

1. Preparation of Nanoparticle Coated Substrates. A schematic diagram of the different steps involved in the fabrication of the nanoparticle self-assembled multilayers on conducting glass substrates is depicted in Figure 1. Briefly, it involves pretreatment of the substrate to make it hydrophilic followed by anchoring the desired nanoparticles. The following subsections detail the processes and the procedures followed.

(A) Materials. Preparation of AuNPs and AuNRs were done using a bottom-up approach with $HAuCl_4 \cdot 3H_2O$ as the precursor. $HAuCl_4 \cdot 3H_2O$, cetyltrimethylammonium bromide (CTAB), and ascorbic acid were purchased from CDH, India. $AgNO_3$, 3-aminopropyltriethoxy silane (APTES), and 1,6 hexanedithiol (HDT) were from Sigma-Aldrich. Indium doped tin oxide (ITO) conducting glass substrate for immobilizing the nanoparticles was purchased from Nippon Sheet Glass Ltd and had a resistivity of 40 Ω/cm.

The analyte liquids, such as 2-propanol, acetone, acetonitrile, hexane, and toluene, were purchased from local sources and distilled prior to use. Triply distilled water was used throughout the experiments.

(B) Synthesis of Au/Ag@Citrate Nanoparticles. AuNPs with mean diameters of 15 nm were prepared by reduction with trisodium citrate under boiling conditions, following established procedures.[23] Briefly, 19 mL of an aqueous solution of 5×10^{-3} M of $HAuCl_4 \cdot 3H_2O$ was heated to boiling followed by the addition of 1 mL of a 0.5% (w/w) aqueous solution of trisodium citrate. Boiling was continued till the first appearance of a wine red color, after which the solution was cooled with constant stirring. The final color of the solution was deep wine red. AgNPs nanoparticles having mean diameters 60 nm were also synthesized by a similar method, using $AgNO_3$ as the precursor.

(C) Synthesis of AuNRs. These were synthesized by a seed-mediated method using 4 nm Au nanoparticles.[24] Growth of nanorods occurred due to the slow reduction of Au^{3+} by ascorbic acid in the presence of cetyltrimethylammonium bromide

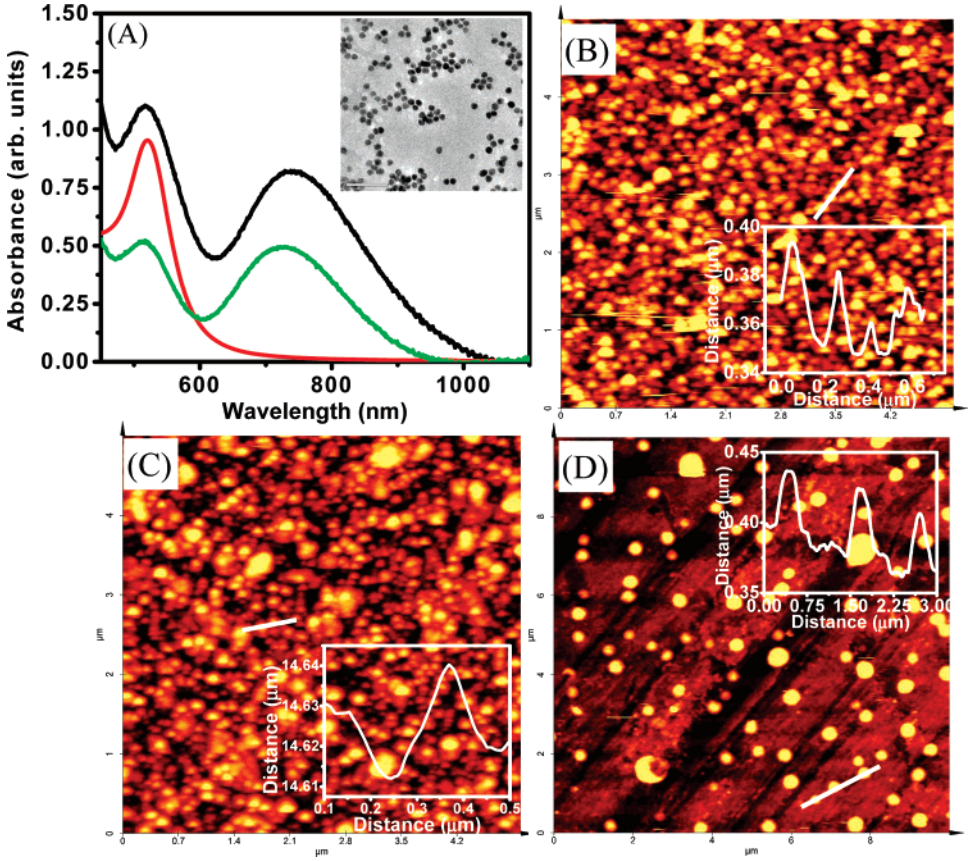

Figure 2. (A) UV−visible spectrum of Au dispersion (red trace) and its assembly on ITO substrate (black trace) and an assembly of AuNRs (green trace). The traces have been normalized to that of AuNPs dispersion. The inset of panel A shows the transmission electron micrograph of the nanoparticles, with the scale bar corresponding to 100 nm. Panels B−D are topographic AFM images of AuNPs, AgNPs, and AuNRs, assembled on ITO substrate, with their height profiles shown as corresponding insets. The images were recorded using contact mode AFM.

(CTAB) as the template. The nanorods synthesized by the above method had an aspect ratio of 2.8. A CTAB double layer stabilized the nanorods.

(D) Cleaning the Substrate. Indium doped tin oxide conducting glass substrates were cleaned with a mild detergent solution to remove greasy impurities. This was then thoroughly cleaned by repeated sonication in deionized water. The substrate, thus cleaned, was dipped in a freshly prepared piranha solution (3:1 ratio of H_2SO_4:H_2O_2) (caution : Piranha solution is a strong oxidizing agent and should be prepared and used with extreme care, avoiding its exposure to all organic reagents) for 1 min and then washed thoroughly with deionized water. Subsequently, the substrate was dipped in 10% (v/v) HCl for 45 min at 80 °C. This was then annealed in a furnace at 450 °C for 8 h.

(E) Functionalization of the Substrate. The clean substrate was dipped in a 30 mM solution of APTES in toluene for 1 h at 80 °C. APTES is known to get both chemisorbed and physisorbed on the substrate. Therefore, the surface thus treated was repeatedly cleaned with toluene to remove the physisorbed APTES. The chemisorbed APTES acts as an anchor to the nanomaterials. The substrate was then dried at room temperature and preserved in a desiccator until further use. The plates stored thus were found to be stable for a week.

(F) Self-Assembly of Nanoparticles on a Functionalized Substrate. The functionalized substrate was dipped in an as-prepared dispersion of AuNPs/AgNPs/AuNRs to have the anchoring of the respective nanomaterials. The dipping time was varied from 20 min for AuNPs to 6 h for AuNRs. The substrate was then cleaned with water and exposed to the spacer molecule. This was done by dipping it in a 30 mM toluene solution of HDT (spacer molecule) for 1 h. The spacer molecules are used to achieve control over the surface coverage of the nanomaterials. One thiol group of HDT covalently attaches to the nanoparticle/nanorods surface exposing the other thiol group for further attachment of nanoparticles/nanorods. Thus, the surface coverage of such multilayer arrays can be tuned to the desired extent. Cleaning the substrate in toluene was carried out to remove the unabsorbed impurities. Repeated dipping in gold nanoparticles/nanorods dispersion and HDT was done to obtain the desired surface coverage.

2. Characterization of the Multilayer Assembly. The formation of the nanoparticle assembly on the substrate was confirmed by UV-vis spectroscopy. UV−vis spectroscopy of the AuNPs dispersion, carried out using a Perkin-Elmer Lambda 25 UV−vis spectrometer, showed a plasmon resonance at 520 nm (Figure 2A). Similar measurement on the AuNPs immobilized substrate exhibited a surface plasmon resonance feature at 524 nm[25] along with a second feature at 720 nm. The latter peak, usually not observed in the solution state, is due to the plasmon coupling between the neighboring nanoparticles. Similar data for AgNPs and AuNRs are provided in the Supporting information (Figures S1 and S2). The nanoparticle assembly was found to be stable to all of the analytes reported here. This was confirmed by recording UV−vis spectra at every stage of the experiment and comparing it with the one recorded at the beginning of the experiment. The traces showed only minor shifts in the surface plasmon peak (<5 nm) confirming the stability of the nanoparticle assembly to the analytes used. No change in intensity after the experiments suggested that the nanoparticle assembly was retained on the substrate.

Contact mode AFM was carried out for better characterization of the substrate using a WiTec GmbH confocal micro Raman setup equipped with a special objective for mounting a silicon cantilever. Topographic images of such an assembly also show the presence of individual particles of 15 nm diameter along with a small fraction of aggregates (Figure 2B). Figure 2B−D presents the contact mode AFM images of Au, Ag, and AuNR multilayer assemblies, respectively, on an ITO surface with their height profiles given as corresponding insets. The full width at half-maximum of these line scans are 17, 80, and 300 nm for panels B−D, respectively. These values are in good agreement with those elucidated from TEM and UV−vis absorption spectra for Au and Ag nanoparticles. The value in the case of AuNR exceeds that observed in TEM, possibly due to the longitudinal aggregation of AuNRs on the substrate. Transmission electron microscopy (JEOL 3010, operating at 300 kV) of the parent AuNPs showed isolated 15 nm particles shown in the inset of Figure 2A. Similar images were observed for silver nanoparticles also (Figures S1). As prepared AuNRs were also characterized by TEM (Figure S2). The rods were of 13 nm diameter and 36 nm length (average dimensions) which showed transverse and longitudinal plasmon resonances at 522 and 724 nm.

3. Electrical Measurements. An assembly thus fabricated was used to construct the sensor device. The device consists of two ITO substrates, one of which is functionalized with the nanoparticles. The two substrates were held with their conducting sides facing each other, separated by a narrow insulator (of thickness 150−200 μm) at the edges. This creates a channel through which any desired liquid could be passed. Electrical leads are taken from the conducting sides of both the plates and connected to a Keithley 2700 digital multimeter-data acquisition system. This is interfaced with a computer which enables automatic data acquisition and storage. The entire device was suspended inside a cylindrical glass column having a 22 mm inner diameter and 36 cm length. A peristaltic pump regulates the flow of the desired liquid from the bottom of the device to avoid air bubbles. A schematic of the experimental setup is shown in Figure 3.

A typical experiment starts with the flow of the desired liquid through the cylindrical column at a specified rate using the peristaltic pump. The potential difference generated between the two substrates, in a direction transverse to the flow, was measured by the Keithley 2700 data acquisition system. Shielded electrical leads from the conducting surfaces of the two substrates, constituting the device, are connected to the multimeter and interfaced to the computer to allow for automatic data acquisition (Figure 3). The electrical connections were externally shorted at periodic intervals, and the substrates were brought to ground potential. The release of the shorting causes the potential to increase and stabilize after the initial transient response. This sequence from one shorting to the next constitutes one cycle of the measurement, during which time the potential saturated. Several such cycles were measured for each variation in experimental parameter. This was done to ensure reproducibility of the observed results and also to estimate the error associated with the measurements. Each cycle consisted of a transient time (∼200 s) followed by a stabilization time (∼2000 s, this being an order of magnitude higher that the transient time scale). An enlarged portion of a single cycle has been given in the inset. The large transient time indicates slow processes involved in building the potential difference in the system. The transient time scale is not very sensitive to different experimental conditions. However, no deterioration in the magnitude of the stabilized response was observed even after 24 h of continuous

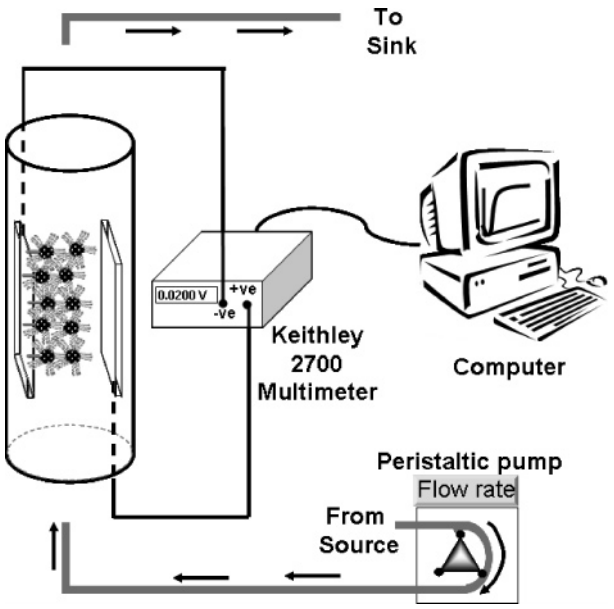

Figure 3. Schematic of the experimental setup (not to scale). The two ITO substrates are arranged with their conducting sides facing each other and separated by an insulating spacer. The nanoparticle coated substrate is connected to the negative terminal of the multimeter. The arrows represent the direction of flow, with the broken lines showing the electrical connections to Keithley 2700 digital data acquisition device.

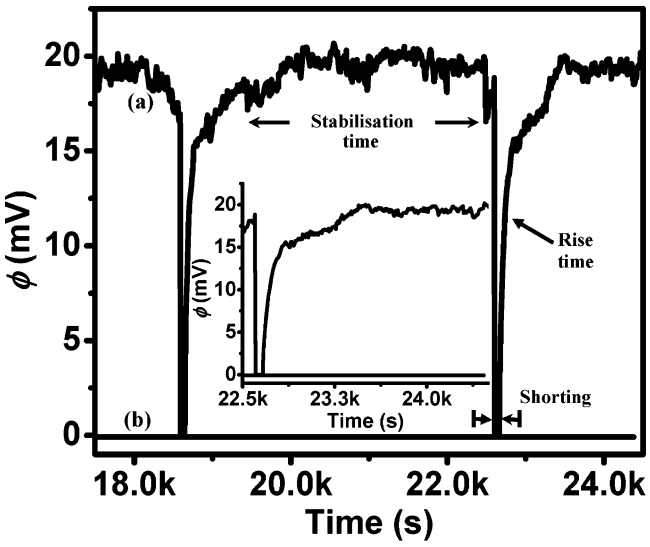

Figure 4. Expanded view of (a) the response of the device containing AuNPs to a flow rate of 500 cm^3/h and (b) the potential generated in the streaming direction. The shorting time and stabilization times are indicated. Inset: Detailed dataset showing the rise and stabilization of the response after shorting. The response shown here corresponds to the plate whose UV−vis spectrum and AFM data are presented in Figure 2 and represents a unit of surface coverage.

operation of the device. Figure 4 illustrates two such cycles for a typical measurement. The stabilized potential difference ϕ, averaged over ten such cycles was taken as the instrument response for a given experimental condition. The standard deviation over the cycles indicates the error in the measurement of ϕ. The TEK, namely, ϕ of the order of several tens of millivolts was generated across the two substrates, transverse to the flow, when liquid flows through them.

The volume of liquid flowing per unit time is taken to be V, with the area of cross section of the cylindrical column housing the device to the A. The velocity of the liquid through the

cylinder is estimated to be $u = V/A$. The Reynolds number, calculated for different values of u (varying from 0.01 to 0.05 m/s), ranges from 25 to 125, well below the turbulence limit of 3000. In such a condition, the velocity of the liquid within the device will be proportional to u. Error in the flow rate was also estimated separately by measuring the volume of water for a given period of time, repeated five times for every flow rate.

III. Experimental Results

We perform several test experiments to confirm that the TEK is qualitatively different from known electrokinetic effects. Experiments, conducted to measure longitudinal/streaming potential difference across the two ends of the same substrate, show no significant response in the longitudinal direction, unlike normal electrokinetic effect. We illustrate the role of the flowing liquid and the nanomaterial assembly in the observed TEK. When the flow of the liquid was stopped, the potential drops to a small value $\phi \sim 2-3$ mV. The potential, therefore is due to the flow of the analyte liquid. Any difference in the electrical layer of the two substrates (due to the presence of nanoparticles in one of them) leading to the generation of the potential difference can also be ruled out due to the nonobservance of this without any flow. To further confirm this, a sputter coated Au(111) surface was used instead of the nanoparticle-coated substrate, and the flow was made keeping all other conditions identical. The potential observed in this case was comparable to that obtained without flow. It is also observed that, when the substrate containing the nanoparticles/nanorods was connected to the negative of the Keithley 2700 multimeter, a positive potential difference was registered. The terminals of Keithley were checked and labeled using a commercial dry cell. Thus, it became evident that a charge buildup was occurring on the substrate containing the nanoparticles.

We carried out measurements for a couple of different situations: (A) both the substrates without the nanoparticles and (B) both the substrates containing nanoparticles of similar surface coverage. There was an approximately 2 mV potential difference observed in these cases. Further, the potential difference was not found to vary with changes in the flow rate or other flow parameters. In a separate experiment, an array of silica nanoparticles was fabricated on an ITO substrate. A device made with such a substrate failed to respond to the analyte flow. Thus, all of these control experiments point toward the development of a TEK due to the presence of a metal nanoparticle assembly.

Figure 5 shows a ϕ versus u plot with three distinct regions of dependence:[26] (i) A low flow rate regime, from 100 to 250 cm^3/h, showing a slow dependence of potential difference on the flow rate, (ii) a mid-flow rate regime, between 250 and 400 cm^3/h exhibiting a sharper dependence, and (iii) a high flow rate regime, from 400 to 500 cm^3/h, showing a saturation of the potential difference. Note that the relative error in the measurements is much less for higher flow rates. Thus, the potential difference as a whole has a sigmoid shape. The previous report does not show three regions distinctly due to limited number of data points in u.

We illustrate the sensitivity of ϕ to various experimental parameters such as the dipole moment and the viscosity of the analyte liquid, the ionic concentration in the analyte liquid, and the surface coverage of the nanomaterials on the substrate. The error in potential difference decreases as the flow rate is increased. With the error in the flow rate also following the same pattern, it is safe to conclude that much of the error in the potential difference can be traced back to minor irregularities

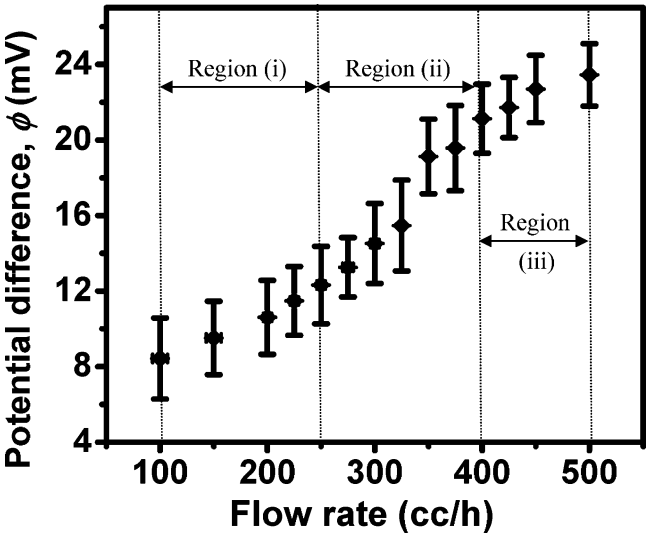

Figure 5. Plot of potential difference versus flow rate of the analyte liquid (water). The ϕ dependence on flow rate has been divided into 3 regimes, as discussed in the text.

in the flow rate. Thus, the system has the least error for a flow rate of 500 cm^3/h, and therefore, this particular flow rate was chosen to study the effect of other parameters on the potential difference generated.

(A) Dipole Moment, μ, of the Analyte Liquid. The liquids used for studying the effect of dipole moment are tetrahydrofuran (1.66 D), ethyl acetate (1.78 D), water (1.8 D), acetone (2.88 D), and acetonitrile (3.92 D). These liquids were used as analytes due to the following reasons: (1) The nanoparticle assembly is found to be unreactive and stable to these liquids. (2) These liquids had comparable viscosities, and therefore, its effect on the observed potential difference can be neglected. Figure 6A shows that ϕ falls with increasing dipole moment. However, with nonpolar liquids like toluene and cyclohexane of comparable viscosity, we do not observe a stabilized voltage response after the initial transients.

(B) Viscosity, η. Varying volumes of methanol and water, having comparable dipole moments, were mixed to obtain different viscosities ranging from 0.5 (for pure methanol) to 0.9 mPa s (for pure water). The viscosity of the mixture was estimated by the average of the viscosities of the individual components[26] according to the composition. Figure 6B shows corresponding ϕ data. There was a linear increase in the ϕ observed with increasing η in the lower viscosity regime. However, ϕ decreases for $\eta \geq 0.80$ mPa s. Even higher viscosity ranges were probed using 2-propanol−water mixtures where the components have comparable dipole moments. Here, as shown in the inset of Figure 6B, ϕ drops with increasing η.

(C) Effect of Salt. For studying the variation of potential difference with ionic concentration, varying concentrations of trisodium citrate in water were used. The choice of the salt was dictated by the stability of the nanoparticle array toward the constituent ions. Figure 6C shows the semilog plot of potential generated as a function of ionic concentration of trisodium citrate. The trend follows a steeply decreasing one, with increasing concentration of ions in the solution.

(D) Surface Coverage. Different surface coverages were achieved by increasing the number of alternate exposures to an aqueous dispersion of AuNPs and ethanolic solution of HDT. These substrates were subsequently studied using contact AFM, to estimate the number of nanoparticles present on the surface per unit area. The responses from these substrates, for a flow rate of 500 cm^3/h of water, are presented in Figure 6D.

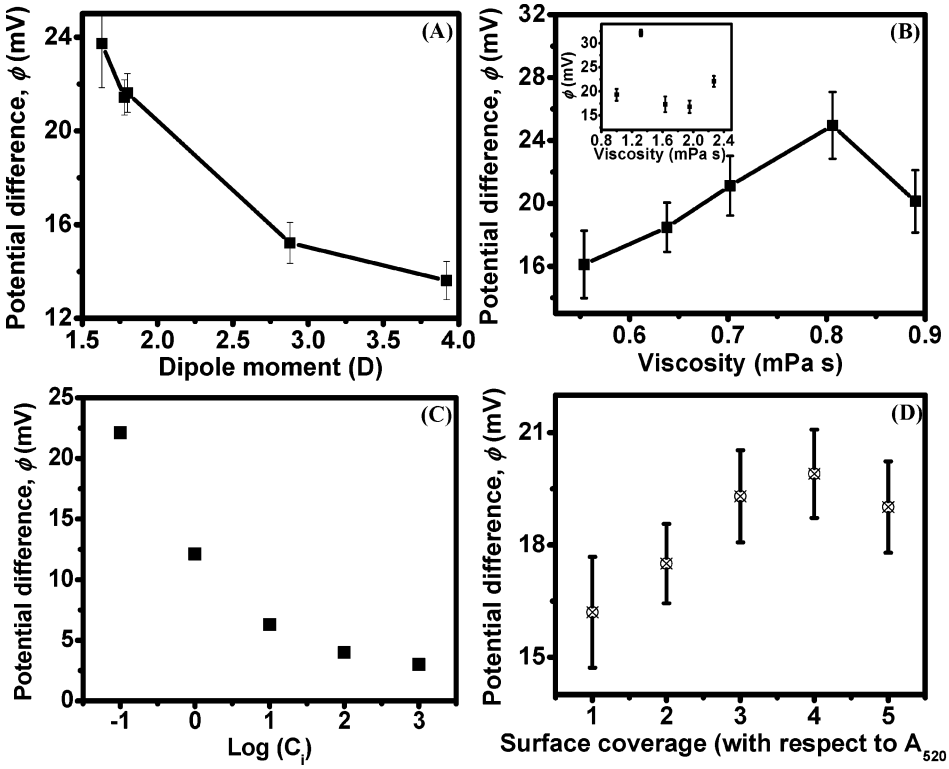

Figure 6. Plot showing the variation of potential difference with (A) dipole moment, (B) viscosity, and (C) ionic concentration of the flowing liquid. The effect of surface coverage of gold nanoparticles on the potential difference generated is shown in panel D. The unit of surface coverage is as given in the caption of Figure 4. Various concentrations of trisodium citrate were used in panel C, whereas viscosities from 0.5 to 0.9 mPa s were achieved by using varying proportions of methanol and water. The inset of panel B shows the trend in the higher viscosity regime, obtained by using 2-propanol and water.

To study whether the phenomenon could be generalized to other metallic nanostructures, AgNPs and AuNRs were immobilized on ITO substrates. The procedure followed for their attachment to the substrate was very similar to that outlined earlier with small variations in exposure times and concentrations. These substrates were then incorporated in the device, and measurements were conducted by varying the flow parameters. The data obtained with AgNPs and AuNRs show flow rate sensitivity of the TEK as in Au nanoparticles (Figure S3). For coverages similar to gold nanoparticle assembly, silver nanoparticles show a higher magnitude of potential difference. The fall in ϕ with decreasing flow rate is sharper for silver nanoparticles than for gold nanoparticles. AuNR systems show high values of ϕ for remarkably low coverages.

Experiments were also done by flowing gases, like nitrogen and hydrogen. Pure gases as well as those saturated with water vapor at room temperature were used as analyte fluids. Flow of carbon dioxide and argon was also tried. The gas flow rate varied from 6000 to 16000 cm^3/min in each case, with several intermediate flow rates. However, no TEK was observed in any of the cases.

IV. Theoretical Model

The absence of TEK for nonpolar fluids indicates that the dipoles of the analyte liquids play a vital role in the observation of TEK. We illustrate the role of the flowing dipoles and the nanoparticle in TEK via a simple model introduced in ref 1. The charges on the nanoparticle surface can get sufficient energy to be free due to the Coulomb collisions with the flowing dipoles, leaving the nanoparticle charged. We estimate the density of such ejected charges around the charged nanoparticle. The ejected charges will be subject to the Coulomb attraction and the streaming velocity as shown schematically in Figure 7. The competition between these two forces will decide the flux of the charges at the surface of the device.

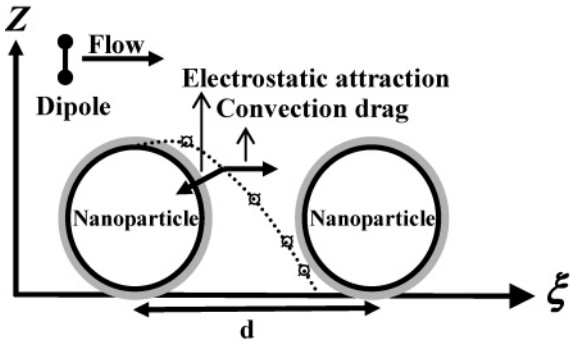

Figure 7. Schematic of the theoretical geometry, illustrating the collision and the subsequent ejection of the charge. The gray shaded region around the nanoparticle represents the surface charges. The dotted line indicates the trajectory of the ejected charge, with the relevant forces indicated.

We consider an isolated nanoparticle immobilized on a substrate. Let the charge on the nanoparticle surface be $-e$ with mass m. Since the second plate in the experimental setup is at a gap L, much larger than the nanoparticle diameter d, we ignore the effect of the second plate. Let us consider a dipole of mass M and dipole moment μ flowing past the nanoparticle at a distance b with velocity u. The geometry is shown in Figure 7. The direction of flow of the dipole is taken to be the ξ axis, and the perpendicular direction is taken to be the z axis. The charge on the nanoparticle surface experiences a time dependent Coulomb field due to the flowing dipole. The components of the time dependent electric field are as follows:

$$E_\xi = \frac{qut}{(b^2 + u^2t^2)^{3/2}} \quad (1a)$$

$$E_z = \frac{qb}{(b^2 + u^2t^2)^{3/2}} \quad (1b)$$

for nonrelativistic situations, namely, $u \ll$ speed of light.[28] The momentum impulse experienced by the charge is given by $\Delta P = -\int_{-\infty}^{\infty} e\vec{E}(t)\, dt$, where the electric field components are given by eq 1a,b. Upon the integration over time, only the z component of the impulse will survive. The energy transferred to the charge is $\Delta\epsilon(b) = 8\mu^2e^2/mb^4u^2$. Note that $\Delta\epsilon(b) \propto 1/u^2\Delta\epsilon(b) \propto 1/u^2$ which is typical for Coulomb collisions.[29] The total energy transferred to the charge $\Delta\epsilon$ due to N_{coll} coherent collisions for dipoles flowing at different distances can be found by integrating over b within the ranges d and L. For $L \gg d$, $\Delta\epsilon = 8\pi N_{coll}\mu^2e^2/\mu^2d^2$. For an average $\langle N_{coll}\rangle \approx 1$, $\Delta\epsilon$ can be comparable to W ($\sim$5 eV), the work function of the charge on the nanoparticle surface. This may lead to the ejection of the charge from the nanoparticle surface with an energy $\Delta\epsilon' = \Delta\epsilon - W$. This will leave the nanoparticle positively charged. The orientation of the flowing dipoles will remain largely unchanged due to the additional polarization effect of the charged nanoparticles. In the gas-phase experiments, the orientation of the dipoles are much more random than that in the liquid-phase such that $\langle N_{coll}\rangle \ll 1$ which fails to eject the charges, and hence, there is no TEK.

The ejected charges will tend to form a bilayer around the charged nanoparticle. Let us now consider the charge density in the bilayer around the charged nanoparticle that will be generated in such collision processes. Note that the ejection of the charge is possible only when $\Delta\epsilon' > 0$. However, the charge with very high energy is unlikely to stay in the vicinity of the nanoparticles. This indicates that at a given temperature T in the vicinity of the nanoparticle, the charge density $\propto \theta[\Delta\epsilon']\exp[-\Delta\epsilon'/k_BT]$, k_B being the Boltzmann constant. Here $\theta[x]$ is a unit step function, namely, $\theta[x] = 1$ for $x > 0$ and $\theta[x] = 0$ for other values of x. The charge ejection is proportional to the number of collisions a given dipole will experience over a certain time scale τ, estimated $\tau \sim Mu/F_{coul}$, where F_{coul} is the typical Coulomb force on the dipole due to the substrate having the charged nanoparticles. If the nanoparticles are not too dense on the surface, the number of collisions is given by $\sigma u\tau$ where σ is the surface coverage of the nanoparticles. However, due to the presence of adjacent nanoparticles which could be charged, some of the ejected charges will undergo recombination with the neighboring nanoparticle. The number of such recombination is given by $\sigma^2 g(d) u\tau^2$ where $g(d)$ is the probability that two nanoparticles will be at a separation d on the surface. $g(d) = 1$, if the nanoparticles are uncorrelated on the surface. Any deviation from unity would imply correlation in the nanoparticle distribution. The net charge density considering the recombination effect is given by

$$\rho_c = (\pi\sigma/V)(M/F_{coul}d)[1 - \sigma g(d)]\,\theta[\Delta\epsilon']\exp[-\Delta\epsilon'/k_BT] \quad (2)$$

V being the volume of the system.

The charges in the bilayer around the nanoparticle will undergo distortion due to the streaming motion as shown in the schematic diagram of Figure 7. The voltage developed between the two plates is proportional to the flux of the charges at the surface to which the nanoparticle is anchored. This flux is given by $J = \rho_c v_s$, where v_s is the velocity of the charge at the surface. The potential difference generated between the plates $\sigma \propto J$. It is clear from eq 2 that $\rho_c = 0$ arises in two situations:

(i) ρ_c, i.e., without any nanoparticle on the surface, and

(ii) $\sigma = 0$, i.e., for large surface coverage by the nanoparticles.

Both of these are consistent with the experimental observations. Further, the step function implies that there is a critical dipole moment $\mu_c \propto u\sigma^{1/2}$ required in order to have a finite J. This is qualitatively consistent with the experimental observations that nonpolar fluids do not show any TEK. Note that J falls off with increasing d which implies that the TEK is unlikely to be strong for large sized nanoparticles. If the surface area exposed to collision with the flowing dipoles is larger, TEK will be more prominent which is consistent with our observations on AuNR systems.

The charged bilayer will undergo distortion due to streaming. Since the saturation time scale in the experiments is quite large, the charge would get solvated in the dipolar medium. We then consider an effective carrier with a net electronic charge which we treat classically. The velocity v_s of the solvated charge after ejection has been calculated within the overdamped limit in the same way as in ref 1. The electrostatic interaction V_{el} of the charged carrier and the charged nanoparticle of net charge Ze has been calculated introducing an appropriate electrostatic image[28] to take care of the metallic boundary condition on the nanoparticle surface. We ignore the polarization of the medium due to the charged carrier and the charged nanoparticle. Further, we ignore the screening of the electrostatic interaction due to the bilayer. The electrostatic force will compete with the streaming velocity so far as it is not too large, the dominant competing forces being indicated schematically in Figure 7. As in ref 1, we take additional systematic forces on the charged carrier: (1) The force of interaction with the flowing dipole with velocity u, given by $-e\vec{E}$ with components, $E_\xi' = [3n_\xi(n_\xi\mu) - \mu]/[(z + b)^2 + (\xi + ut)^2]^{3/2}$ and $E_z' = [3n_z(n_z\mu) - \mu]/[(z + b)^2 + (\xi + ut)^2]^{3/2}$, where the unit vector components are $n_\xi = (\xi + ut)/[(z + b)^2 + (\xi + ut)^2]^{3/2}$ and $n_z = (z + b)/[(z + b)^2 + (\xi + ut)^2]^{(3/2)}$. (2) A steeply repulsive interaction to ensure that the ejected charge carrier cannot penetrate the core of the nanoparticle after ejection: $V_{rep} = V_{rep}^0/r^{12}$, V_{rep}^0 being the magnitude of the repulsion at the unit separation. Further, the large saturation time scale ($\sim$ few minutes) involved in the experiments indicates a strong damping of the motion of the charge carriers in the complicated network of the nanoparticles. The thermally averaged overdamped velocity components will be given by

$$\frac{\partial}{\partial t}\langle\xi\rangle = -\left\langle\frac{1}{\Gamma}\left[-eE_\xi' + \frac{\partial(V_{el} + V_{rep})}{\partial\xi}\right]\right\rangle + u \quad (3a)$$

and

$$\frac{\partial}{\partial t}\langle z\rangle = -\left\langle\frac{1}{\Gamma}\left[-eE_z' + \frac{\partial(V_{el} + V_{rep})}{\partial z}\right]\right\rangle \quad (3b)$$

Γ is the phenomenological damping coefficient.[28] We expand the force components about the mean and retain only the first term in the expansion as in mean field approximations. The resulting set of equations are solved numerically to obtain with the initial conditions that, at $\langle\xi\rangle = d^*/2$, $\langle z\rangle = d^*$ at $t = 0$ and obtain, $v_s^* = \{[(d/dt)\langle\xi\rangle]^2 + [(d/dt)\langle z\rangle]^2\}^{1/2}$, d^* being the diameter of the nanoparticle.

We choose the length unit of $l = 10^{-7}$ cm, a typical nanoscale, the time unit of s, a typical diffusion time of a molecule in the still analyte liquid and energy unit, $\gamma = 10^{-6}$. Figure 8 shows

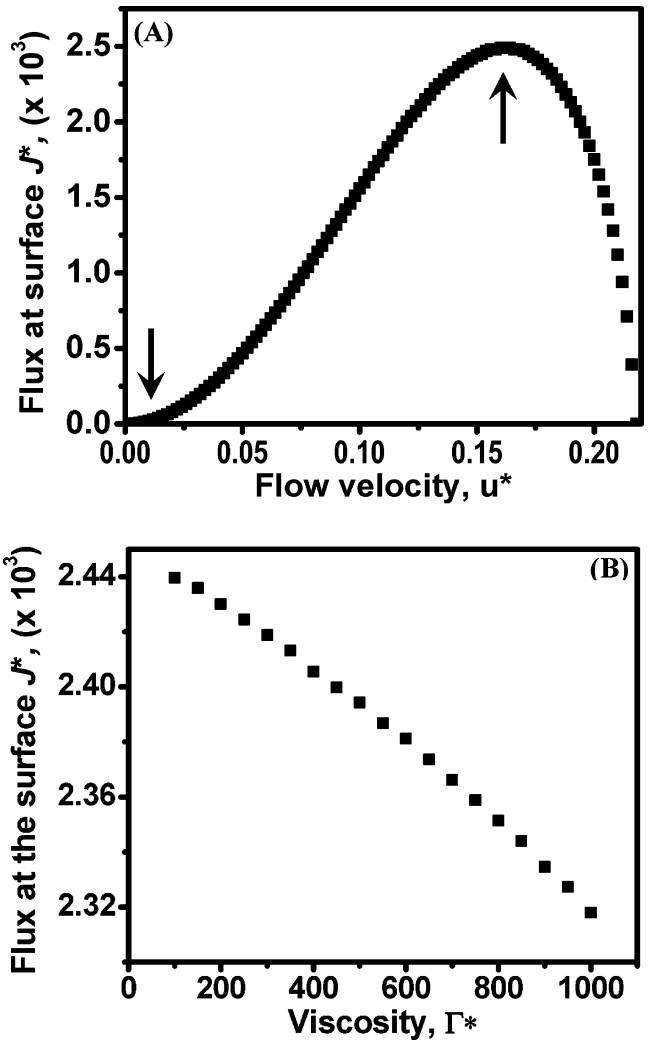

Figure 8. Plot showing the dependence of J^* on u^* (A) and Γ^* (B) The arrows indicate the experimentally relevant regime of flow rates.

J^* as a function of $u^* = u\tau/l$. We find that J^* increases with u^* for small u^*. This can be understood by the fact that the Coulomb collisions can impart more energy for small u^*. For large u^*, due to less efficient Coulomb collisions, $\rho_c \rightarrow 0$, which leads to a maximum in J^*. Note that the maximum position agrees reasonably well to the experimental number where the large u saturation of J^* takes place. The onset of the maximum where the change in the flux with the flow velocity slows down may appear as a saturation in the experimental situations. In fact, below the maximum, the shape of the curve resembles that of Figure 6 indicating an overall good semiquantitative agreement. We find that J^* decreases with Γ^* ($=\Gamma/ml\nu^{-2}$) as shown in Figure 8B. This trend is similar to that of n in the large limit in Figure 6B.

V. Conclusions

In summary, a novel transverse electrokinetic effect is demonstrated. This is due to the flow of liquids over a nanoparticle assembly and is manifested as a potential difference. The dependence of the potential on parameters like the flow velocity, dipole moment, viscosity, and ionic concentration of the flowing liquids are studied. Using these inputs, a semiquantitative model is proposed, wherein the flowing dipole interacts with the surface charges on the nanoparticle. Such Coulomb interaction leads to the ejection of charges from the nanoparticle surface. The flux at the surface of the substrates is numerically estimated. The variation of this flux with flow velocity and viscosity is found to be in excellent agreement with that observed experimentally. Besides, such a model also brings in the concept of a critical dipole moment of the flowing liquid above which such an effect is observed. The same phenomenon is seen in other metallic nanostructures. The reproducible signal, dependence on the flowing liquid, and its inherent parameters with scope for miniaturization are seen as huge advantages for the applicability of this device, particularly in the context of biological flow channels.

Acknowledgment. T.P. thanks the Department of Science and Technology (DST), Government of India for financial support. Instrumentation was supported by the Nanoscience and Nanotechnology Initiative of the DST. C.S. acknowledges a research fellowship from CSIR.

Supporting Information Available: UV−vis spectrum and TEM images of Ag nanoparticles, TEM images of Au nanorods, TEK for Ag nanoparticle, and AuNR assemblies. This material is available free of charge via the Internet at http://pubs.acs.org.

References and Notes

(1) Subramaniam, C.; Pradeep, T.; Chakrabarti, J. *Phys. Rev. Lett.* **2005**, *95*, 0164501.
(2) Kim, Y.; Johnson, R. C.; Hupp, J. T. *Nano. Lett.* **2001**, *1*, 165.
(3) Storhoff, J. J.; Lucas, A. D.; Garimella, V.; Bao, Y. P.; Muller, U. R. *Nat. Biotechnol.* **2004**, *22*, 883.
(4) Vo-Dinh, T.; Yan, F.; Wabulyele, M. B. *J. Raman Spectrosc.* **2005**, *36*, 640.
(5) Schultz, D. A. *Curr. Opin. Biotechnol.* **2003**, *14*, 13.
(6) Vossmeyer, T.; Guse, B.; Besnard, I.; Bauer, R. E.; Mullen, K.; Yasuda, A. *Adv. Mater.* **2002**, *14*, 238−242.
(7) Dobkin, D. *Principles of chemical vapor deposition*; Kluwer Academic Pub.: Norwell, MA, 2003.
(8) Choudhury, B.; Shinar R.; Shinar, J. *J. Appl. Phys.* **2004**, *96*, 2949−2954.
(9) Payne, M. M.; Parking, S. R.; Antony, J. E.; Kuo, C.-C.; Jackson, T. N. *J. Am. Chem. Soc.* **2005**, *127*, 4986−4987.
(10) Kumar, A.; Abbott, N. L.; Biebuyck, H. A.; Kim, E.; Whitesides, G. M. *Acc. Chem. Res.* **1995**, *28*, 219−226.
(11) Kim, E.; Whitesides, G. M. *Chem. Mater.* **1995**, *7*, 1257.
(12) Nath, N.; Chilkoti, A. *Anal. Chem.* **2002**, *74*, 504.
(13) Basabe-Desmonts, L.; Beld J.; Zimmerman, R. S.; Hernando, J.; Mela, P.; Garcia Parajo, M. F.; van Hulst, N. F.; van der Berg, A.; Reinhoudt, D. N.; Crego-Calama, M. *J. Am. Chem. Soc.* **2004**, *126*, 7293.
(14) Mark. S. S.; Sandhyarani, N.; Zhu, C.; Campagnolo, C.; Batt, C. A. *Langmuir* **2004**, *20*, 6808.
(15) Nguyen, N. T. *Flow Meas. Instrum.* **1997**, *8*, 7.
(16) Yan, D.; Nguyen, N.-T.; Yang, C.; Huang, X. *J. Chem. Phys.* **2006**, *124*, 021103.
(17) Yang, J.; Lu, F.; Kostiuk, L. W.; Kwok, D. Y. *J. Micromech. Microeng.* **2003**, *13*, 963.
(18) van der Hayden, F. H. J.; Bonthuis, D. J.; Stein, D.; Meyer, C.; Dekker, C. *Nano. Lett.* **2006**, *6*, 2232.
(19) Ghosh, S.; Sood, A. K.; Kumar, N. *Science* **2003**, *299*, 1042.
(20) Sood, A. K.; Ghosh, S. *Phys. Rev. Lett.* **2004**, *83*, 086601. Ghosh, S.; Sood, A. K.; Ramaswamy, S.; Kumar, N. *Phys. Rev. B* **2004**, *70*, 205423.
(21) Kral, P.; Tomanek, D. *Phys. Rev. Lett.* **1999**, *82*, 5373. Wang, B. Y.; Kral, P. *J. Am. Chem. Soc.* **2006**, *128*, 15984.
(22) Schasfoort, R. B. M.; Schlautmann, S.; Henddriske, J.; van der Berg, A. *Science* **1999**, *286*, 942−945.
(23) Turkevich, J.; Stevenson, P. L.; Hiller, J. *Discuss. Faraday. Soc.* **1951**, *11*, 55.
(24) Sau, T. K.; Murphy, C. J. *Langmuir* **2004**, *20*, 6414.
(25) Sandhyarani, N.; Pradeep, T. *Int. Rev. Phys. Chem.* **2003**, *22*, 221.
(26) In our earlier report, we monitored the trend of ϕ with u for every 100 cc/h change. On the basis of this, we predicted a linear dependence of potential difference on the flow rate.
(27) *CRC Handbook of Chemistry and Physics*, 84th ed.; Lide, D. R., Ed.; CRC Press: Boca Raton, FL, 2003.
(28) Jackson, J. D. *Classical Electrodynamics*; John Wiley & Sons Inc.: New York, 1999.
(29) Chaikin, P. M.; Lubenski, T. C. *Principles of Condensed Matter Physics*; Cambridge University Press: New York, 1995.